Water Practice & Technology

IWA PUBLISHING

Water Practice & Technology Vol 19 No 10, 4267 doi: 10.2166/wpt.2024.237

Adsorption of methylene blue onto clay/carbon composite: kinetics and isotherms study

Freeman Madhau[a,b], Zhenjun Wu[a,c], Yahui Shi[a,c], Dongjin Wan[a,c,*], Shepherd Tichapondwa[d], Yangyang Wang[a], Jiekai Wang[a] and Heyu Wan[a]

[a] College of Environmental Engineering, Henan University of Technology, Zhengzhou, Henan 450001, China
[b] Department of Water Resources Engineering, Bulawayo Polytechnic, P.O. Box 1392, Bulawayo, Zimbabwe
[c] Zhengzhou Key Laboratory of Water Safety and Water Ecology Technology, Zhengzhou, Henan 450001, China
[d] Water Utilization and Environmental Engineering Division, Department of Chemical Engineering, University of Pretoria, Pretoria 0002, South Africa
*Corresponding author. E-mail: djwan@haut.edu.cn

DW, 0000-0003-4656-5544

ABSTRACT

Waste treatment for pollution control is a hot topic being studied and has received growing attention. In this study, spent bleaching earth (SBE), a waste material from the oil refineries, was pyrolyzed in a N_2 atmosphere to produce an environmentally sustainable clay/carbon composite (SBE@C (500 °C)). SBE@C (500 °C) was tested for its ability to remove methylene blue (MB) from water. The Langmuir model best explained the adsorption isotherms, with maximum adsorption capacity of 29.54 mg/g (MB solution (10–60 mg/L)). The pseudo-second-order kinetic model effectively described the adsorption kinetics data. Thermodynamic parameters indicated spontaneous and endothermic processes. The impact of coexisting cations on MB adsorption by SBE@C (500 °C) decreased in the following order: $Fe^{3+} > Al^{3+} > Mg^{2+} > K^{+} > Na^{+}$. The ionic strength results indicated that increasing the concentration of Na^{+} ions led to a decrease in adsorption capacity. MB removal was greatest at pH level of 8. The adsorption mechanisms involved π–π interactions, electrostatic interactions, and changes in physicochemical properties. After 3 cycles, SBE@C (500 °C) may be recycled up to 11 times before completely losing its adsorption capacity. Overall, SBE@C (500 °C) shows promise for removing MB from wastewater, while mitigating secondary pollution from SBE.

Key words: adsorption, isotherms, kinetics, methylene blue, spent bleaching earth

HIGHLIGHTS

- SBE@C (500 °C) was prepared by pyrolysis using SBE.
- Pyrolysis significantly increased the specific surface area of SBE from 0.17 to 68.28 m^2/g.
- SBE@C (500 °C) adsorption capacity was 2.78 times that of SBE at 45 °C.
- Fe^{3+} and Al^{3+} have a more inhibitory effect on MB adsorption by SBE@C (500 °C).
- Adsorption mechanisms: π–π interactions, electrostatic interactions, and changes in physicochemical properties.

GRAPHICAL ABSTRACT

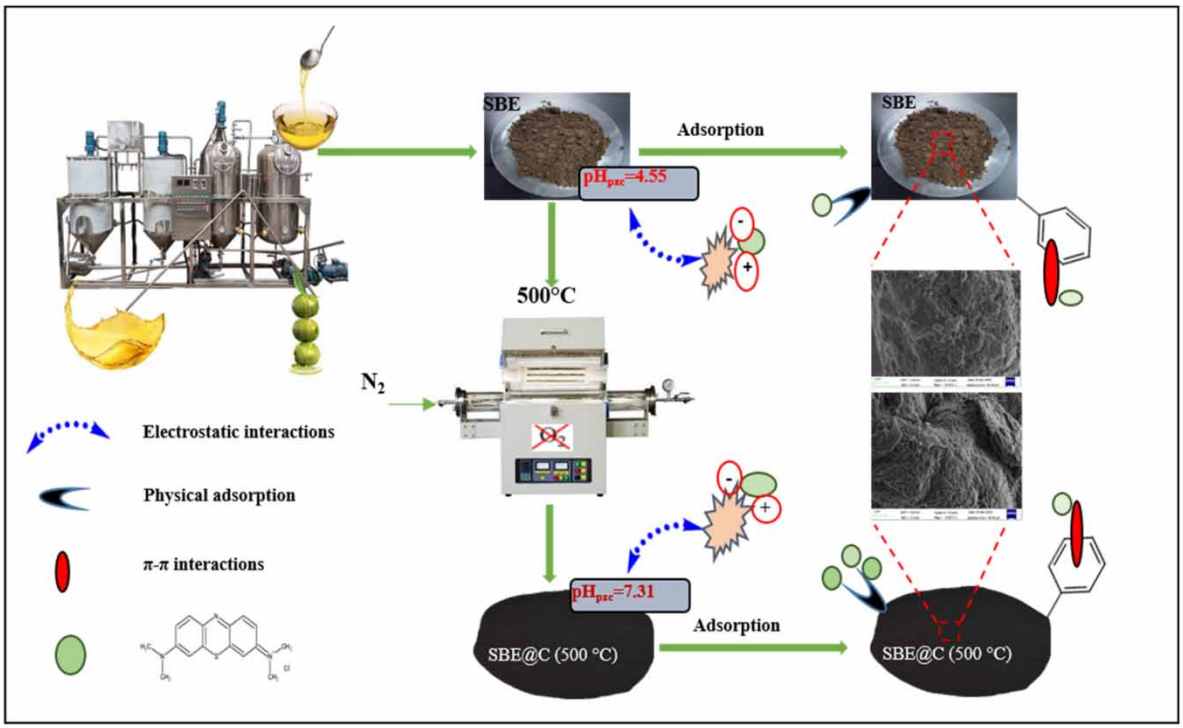

1. INTRODUCTION

Recently, increasing attention has been given to the technology for removing organic colorants (dyes) from wastewater (Nurani *et al.* 2024). The presence of organic dyes in wastewater is visually unappealing even at minimal concentrations and may exert a substantial inhibitory effect on the photosynthetic rate of aquatic flora. Methylene blue (MB), classified as a basic thiazine (cationic) dye, holds substantial significance due to its numerous applications, including printing and dyeing, rubber, coloring paper, wool, leather, and dyeing cotton (Duman *et al.* 2020). MB possesses a complex structure with numerous organic groups, and after entering the water, it becomes more stable and difficult to degrade (Qi *et al.* 2020). Acute human exposure to MB can result in increased heart rate, tissue necrosis, yellowing of the skin and eyes, quadriplegia, and vomiting (Alharby *et al.* 2021). Moreover, MB has been reported to be mutagenic and carcinogenic (Lagiewka *et al.* 2023). Hence, the removal of MB dye traces from wastewater becomes environmentally significant.

Various methods are used in wastewater treatment to remove dyes from aqueous systems, including photocatalysis, coagulation or flocculation, environmental bacteria, and physical adsorption, among others (Mohadesi *et al.* 2024). Adsorption is a commonly used method for removing dyes from wastewater. Compared with other methods, adsorption is a more advantageous option due to its low operating costs, minimum waste disposal, and high efficacy. In addition, adsorption techniques do not require sophisticated technologies, design characteristics, or processes to function effectively (Mohadesi *et al.* 2024). Recently, there has been a noticeable increase in the use of activated carbon for pollutant removal from wastewater; nevertheless, this adsorbent is still costly and difficult to regenerate. Several cost-effective adsorbents have been explored for their potential to remove MB dye from wastewater, including cellulose nanocrystals extracted from sugar cane bagasse (Raj *et al.* 2024) and clay (Loutfi *et al.* 2023).

Spent bleaching earth (SBE), a by-product of the oil refinery industry, has the potential to be a useful adsorbent for MB. SBE is mainly composed of aluminosilicate materials of Al_2O_3 and SiO_2 with a percentage of 60–80% and contains oil residue (approximately 20–40 wt.%) and other metal impurities (Abdelbasir *et al.* 2023). SBE is the by-product that remains after the bleaching earth has been decolored during the oil refining process. The improper disposal of SBE into the environment can result in spontaneous combustion in the air and the emission of unpleasant odors, consequently contributing to secondary pollution (Liu *et al.* 2021). Recent research has demonstrated that, by appropriate treatment, SBE can serve as an effective adsorbent material for heavy metals

(Ke *et al.* 2023) or dyes (Liu *et al.* 2021). Treatment methods for SBE include but are not limited to aerobic calcination, acid-base and surfactant modification, and hydrothermal methods. While the aerobic calcination method can release harmful and toxic gases into the environment, the acid-base and surfactant modification causes secondary pollution and, the hydrothermal method, while capable of producing high-quality materials, often suffers from low yield and limited scalability, hindering its practical applications (Wan *et al.* 2021). The calcination of SBE to obtain a clay/carbon composite (SBE@C) has exhibited commendable adsorption capabilities (Wan *et al.* 2019, 2021; Liu *et al.* 2021). Reports of SBE treatment under anoxic conditions are rare, even though this approach is simple to implement and prevents secondary pollution.

In this study, we report the treatment of SBE, a solid waste from oil refineries, to produce SBE@C (500 °C) adsorbent, through pyrolysis under an anoxic environment. The effect of pyrolysis temperature (300–900 °C) on the removal capacity of MB by carbonized SBE was explored. Then, an investigation and comparison of the adsorption properties (kinetics and isotherms) of MB onto SBE or SBE@C (500 °C) were carried out. A comprehensive evaluation assessed the influences of crucial factors such as adsorbent dosage, initial pH, temperature and coexisting cations, and ionic strength on SBE and SBE@C (500 °C). Additionally, the materials were characterized to explore their potential adsorption mechanisms. This research stands out from other studies by examining the original SBE and the clay/carbon composite (SBE@C (500 °C)) in its analysis. Additionally, the study explores the levels of dissolved organic carbon (DOC) released into both pure water and the MB solution after adsorption by SBE and SBE@C (500 °C).

2. MATERIALS AND METHODS

2.1. Chemicals

$C_{16}H_{18}CIN_3S$, HCl, NaCl, $MgCl_2$, $AlCl_3$, $FeCl_3{\cdot}6H_2O$, KCl, and NaOH were all of analytical grade and supplied by Kermel Chemical Reagent (Tianjin, China).

2.2. Synthesis of the SBE@C (500 °C)

SBE was obtained at no cost from United Refineries Limited (Bulawayo, Zimbabwe). The SBE was dried for 24 h, pulverized into a powder, and passed through a sieve of less than 100 mesh, allowing for a maximum particle size of 150 μm. The sifted SBE was subjected to pyrolysis at a programmed heating rate of 8 °C/min. The pyrolysis experiment was conducted at 300, 500, 700, and 900 °C for 2 h under a continuous flow of nitrogen gas at 150 mL/min (Wan *et al.* 2021). The final products marked as SBE@C (300 °C), SBE@C (500 °C), SBE@C (700 °C), and SBE@C (900 °C), were stored in a desiccator before and after each experiment.

2.3. Adsorption kinetics

Adsorption kinetics of a 10 mg/L solution of MB onto 0.6 g/L SBE or SBE@C (500 °C) were performed in a 500 mL flask. The experiments were conducted at 25, 35, and 45 °C using a thermostatic oscillator (ZD-85 Shanghai Lichen, China). A 500 mL volume of MB solution was used, and the mixture was continuously stirred at 150 rpm for 140 min. The MB removal capacity q_t (mg/g) at time t (minutes) was determined using Equation (1):

$$q_t = \frac{(C_0 - C_t)V}{m} \tag{1}$$

where C_0 and C_t (mg/L) denote the initial MB concentration and time t (minutes), respectively, V (L) represents the volume of the MB solution, and m (g) represents the mass of the adsorbent.

2.4. Adsorption isotherms

Adsorption isotherms of a 100 mL MB solution (10–60 mg/L) onto 0.6 g/L for SBE or SBE@C (500 °C) were prepared in a set of 150 mL Erlenmeyer flasks. The solution was then agitated on a thermostatic oscillator (ZD-85 Shanghai Lichen, China) at 150 rpm for 300 min. The research also investigated the impact of temperatures (25, 35, and 45 °C) and conducted concurrent thermodynamic assessments. The pH of the solution was not adjusted during the experiment to ensure that the adsorption process was not influenced by the presence of ions introduced by pH adjustment.

2.5. Adsorbent dosage

Varying adsorbent dosages of SBE@C (500 °C) (0.3–1.5 g/L) were mixed with samples of 10 mg/L (100 mL) MB solution to assess the impact of dosage on MB adsorption. Other experimental conditions were kept constant, including a contact time of 120 min, temperature of 25 °C, pH of 6.5, and mixing speed of 150 rpm. The adsorption reaction was then carried out and samples were taken periodically to ascertain the remaining concentration of MB in solution.

2.6. Effects of initial pH, coexisting cations, and solution ionic strength

An investigation was conducted to assess the impact of initial pH (4–9) on the adsorption of MB solution 10 mg/L, at a dosage of 0.6 g/L for both SBE and SBE@C (500 °C). pH measurements were conducted using a Leici pHS-3C pH meter (China). The pH levels were controlled with NaOH or HCl (0.1 mol/L). Additionally, to simulate real MB wastewater conditions, the impact of different selected cations on MB adsorption by both SBE or SBE@C (500 °C) was investigated. SBE or SBE@C (500 °C) (0.6 g/L) were mixed with a 100 mL MB solution of 10 mg/L containing cations (Na^+, K^+, Mg^{2+}, Fe^{3+}, and Al^{3+} 0.01 mol/L). Different concentrations of Na^+ (0.01, 0.05, and 0.1 mol/L) were investigated to analyze the impact of cationic strength on MB adsorption by SBE and SBE@C (500 °C). The experimental parameters, including initial concentration (10 mg/L), adsorbent dose (0.6 g/L), contact time (120 min), temperature (25 °C), and mixing speed (150 rpm), were kept constant.

2.7. Regeneration of SBE@C (500 °C)

The reusability of the adsorbent SBE@C (500 °C) (referred to as SBE@C (500 °C)-de was evaluated using the desorption method. NaOH (0.1 mol/L) solution was mixed with 1 g/L of the adsorbed SBE@C (500 °C). The mixture was agitated for 24 h on a thermostatic oscillator ZD-85 Shanghai Lichen, China (150 rpm) at 25 °C. The solution was filtered and rinsed multiple times with deionized water until a neutral pH was reached. Subsequently, the sample was subjected to a 12-h drying process at 65 °C in an oven. The regenerated SBE@C (500 °C) was sequentially added to a 10 mg/L MB solution at 25 °C. This regeneration process was repeated three times. The resulting data were utilized to assess how effectively SBE@C (500 °C) could be reused.

2.8. Analysis methods

For the detailed analysis methods used in this research, refer to Supplementary Text 1.

3. CHARACTERIZATION

3.1. Scanning electron microscopy (SEM) and energy-dispersive X-ray spectroscopy (EDS) analysis

Figure 1 shows the scanning electron microscopy (SEM) images (magnification: ×10,000) and energy-dispersive X-ray spectroscopy (EDS) analysis of SBE and SBE@C (500 °C) both before and after the adsorption of MB.

After pyrolysis at a high temperature (500 °C), SBE@C (500 °C) displays a unique sheet-like structure with significant surface pores, potentially enhancing its MB adsorption capacity compared with SBE. In contrast, SBE exhibits a rough and compact surface lacking discernible structural characteristics. The Brunauer–Emmett–Teller (BET) results and the morphological changes in SBE@C (500 °C) are in agreement. However, there was no obvious difference in the morphological structure of SBE or SBE@C (500 °C) before and after the adsorption of MB. As illustrated in Figure 1 and Supplementary Table S4, the EDS results show that C, O, Al, and Si make up the majority of the elements in SBE and SBE@C (500 °C), with very few S and Cl. In comparison to those in SBE, there were varying changes in the percentages of the six components in SBE@C (500 °C). The most notable changes were observed in C and O, which ranged from 49.56 to 58.25% and from 42.33 to 35.21%, respectively. According to the EDS results, both SBE and SBE@C (500 °C) contain C, O, Al, Si, S, and Cl both before and after MB adsorption.

3.2. XRD analysis

To gain deeper insight into the physical properties of SBE and SBE@C (500 °C) both before and after MB adsorption, XRD analysis was conducted as shown in Figure 2(a).

The XRD patterns of the characteristic diffraction peaks show that four different substances were present in the materials where quartz predominated: mica, montmorillonite, quartz, and orthoclase. A previous study also demonstrated the same substances in SBE and SBE@C (500 °C) (Liu *et al.* 2020). As shown in Figure 2(a), the peaks of quartz are found at $2\theta = 20.91$, 26.64, 36.53, 39.66, 42.58, 45.89, 50.13, 60.0, and 68.0° (Zhou *et al.* 2013). Peaks at 29.1, 73.3, and 61.8° are assigned as peaks of montmorillonite;

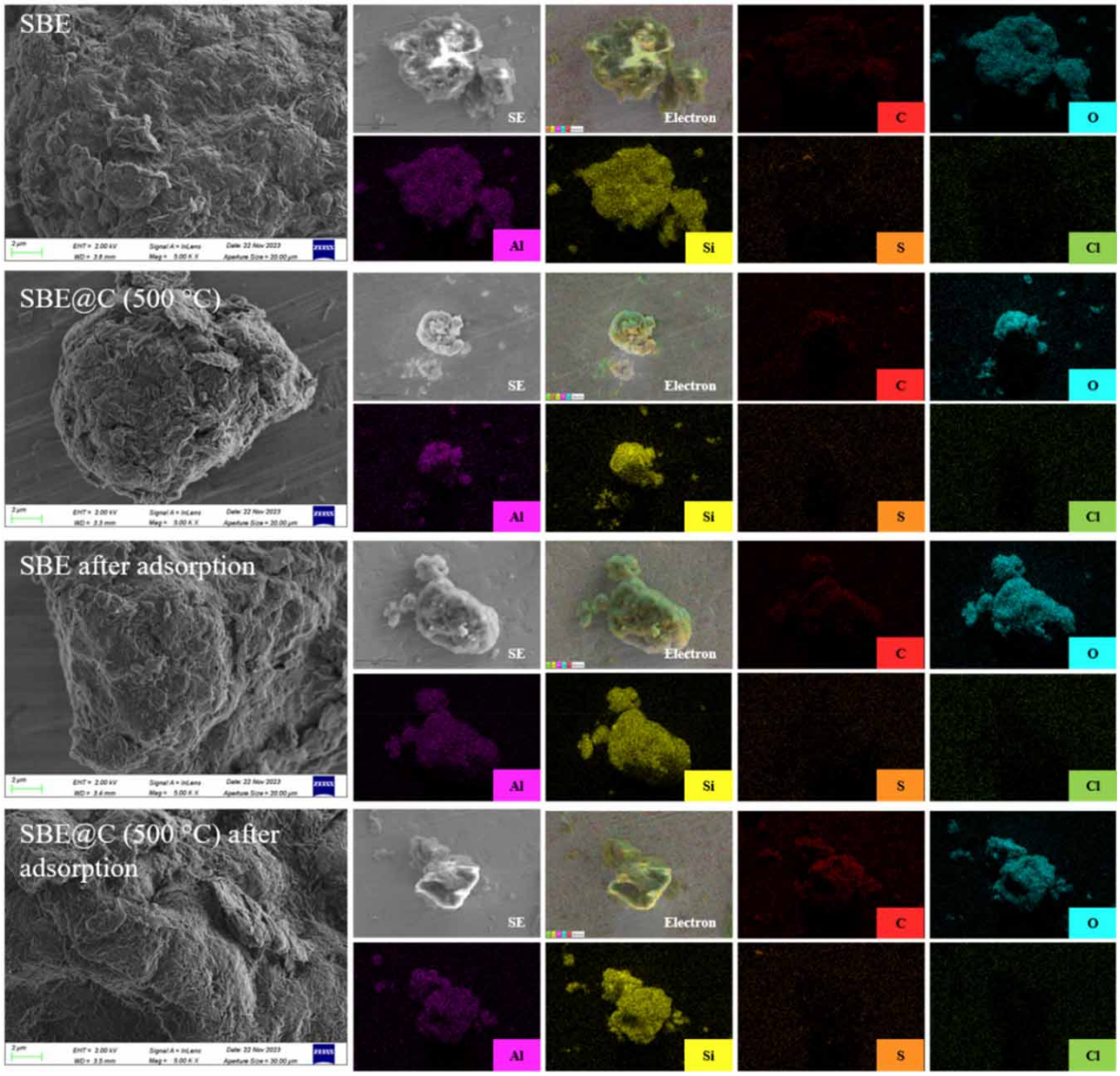

Figure 1 | SEM and EDS analysis of SBE, SBE@C (500 °C), SBE after adsorption, and SBE@C (500 °C) after adsorption.

19.9 and 35.0° indicate the peaks of mica; and the peaks at 23.5, 25.6, and 27.1° are attributed to orthoclase. The similar peaks of SBE or SBE@C (500 °C) both before and after MB adsorption indicate that the structural characteristics of the materials are unaffected by carbonization and adsorption. Compared with SBE@C (500 °C), SBE exhibits similar peaks, but the peaks at $2\theta = 29.1$, 61.8, and 73.3° for SBE@C (500 °C) are notably lower than the SBE peaks. This indicates that SBE@C (500 °C) differs from SBE, which is most likely due to calcination at 500 °C.

3.3. Fourier transform infrared spectroscopy (FTIR) analysis

The Fourier transform infrared (FTIR) spectra of SBE and SBE@C (500 °C) before and after MB adsorption are compared in Figure 2(b). The absorption bands attributed to the organic matter in SBE are at 2,927, 2,855, and 1,466 cm^{-1} (Tang *et al.* 2018). However, these characteristic absorption bands only appeared in SBE and SBE after the adsorption of MB but completely vanished in both SBE@C (500 °C) and SBE@C (500 °C) after the adsorption of MB, showing that high-temperature pyrolysis at 500 °C can fully carbonize the residual organics in SBE. The 1,633 cm^{-1} characteristic absorption band is due to the aromatic stretching vibration of C–H (Wan *et al.* 2019), indicating the presence of aromatic carbon in all the materials. This suggests that the adsorption mechanism of MB onto SBE or SBE@C (500 °C) occurs via π–π interactions. The 1,743 cm^{-1} characteristic absorption band is attributed to the C = O stretching vibration in the carboxyl group (Mana *et al.* 2008).

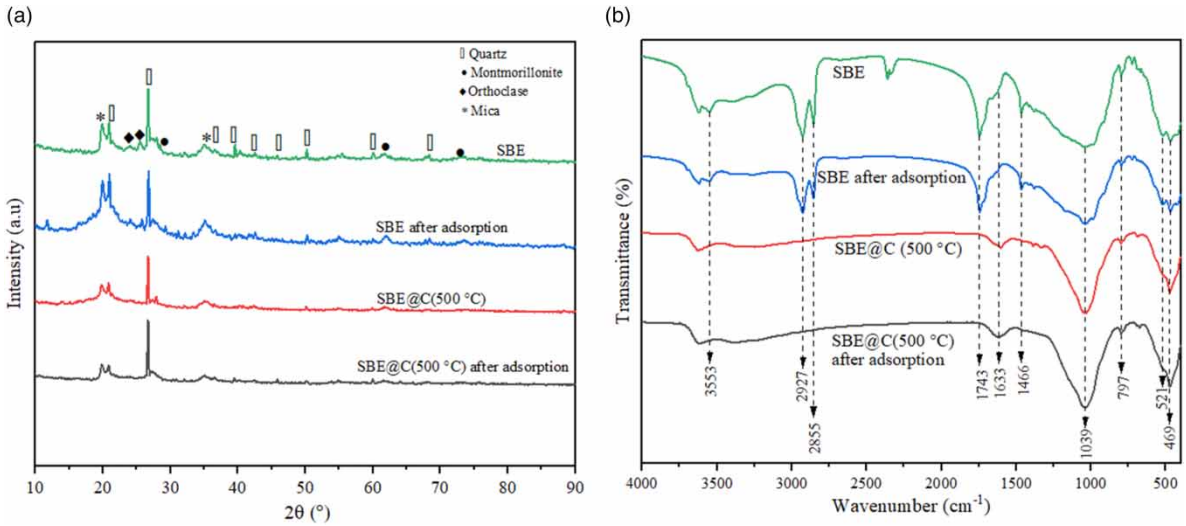

Figure 2 | (a) XRD patterns and (b) FTIR spectra of SBE and SBE@C (500 °C) before and after MB adsorption.

Notably, the characteristic band is visible in SBE and SBE after adsorption but not in SBE@C (500 °C) or SBE@C (500 °C) after adsorption, probably because of its low residual organic matter content. Furthermore, the 3,553 cm^{-1} band is attributed to the –OH group of the absorbed water, and the intensity of this band is significantly weakened in SBE@C (500 °C), which is indicative of dihydroxylation (Kadi *et al.* 2012). The FTIR results indicate that both SBE and SBE@C (500 °C) contain –COOH, –COOR, and –OH groups. The 1,039 and 797 cm^{-1} bands are assigned to the asymmetric and symmetric stretching vibrations of Si–O–Si, respectively, and the 469 cm^{-1} band is due to the bending vibration of Si–O (Christidis *et al.* 1997). Moreover, the absorption band at 521 cm^{-1} is due to the vibration of the Si–O–Al bond (Liu *et al.* 2021). These characteristic absorption bands confirm the interference, which indicates that mica, quartz, and montmorillonite make up SBE and SBE@C (500 °C).

3.4. BET analysis

The pore structure of a material is a key indicator of its adsorption properties. Supplementary Table S5 shows the BET analysis results for SBE and SBE@C (500 °C). Pyrolysis at 500 °C significantly increased the SBE-specific surface area from 0.17 to 68.28 m^2/g. Furthermore, the mesopore volume and average pore diameter of the untreated SBE increased after calcination at 500 °C from 5.82×10^{-4} to 3.4×10^{-1} and 13.83 to 19.93 nm, respectively. This is primarily attributed to the release of volatile organic compounds and oils from SBE during pyrolysis at 500 °C, which significantly enhances the adsorption of MB by SBE@C (500 °C). This is mainly attributable to the release of volatile organic compounds and oils from SBE during pyrolysis at 500 °C and greatly enhances MB adsorption by SBE@C (500 °C).

3.5. X-ray photoelectron spectroscopy (XPS) analysis

Supplementary Figure S5 shows the survey scan and C1*s* X-ray photoelectron (XPS) spectra of SBE and SBE@C (500 °C). Supplementary Figure S5(a) indicates that four main peaks, C1*s*, O1*s*, Si2*s*, and Al2*p*, are present in both materials. To better understand the variations in the XPS spectra between SBE and SBE@C (500 °C), the C1*s* were identified and fitted, as illustrated in Supplementary Figure S5(b) and S5(c). The binding energies at 284.8, 286.7, 287.6, and 289.2 eV correspond to C = C (aromatic carbon group), –C–O (phenolic, alcohol, or either), C–H, and –COOR (ester), respectively (Heymann *et al.* 2011; Wu *et al.* 2014). When comparing Supplementary Figure S5(b) and S5(c), significant differences were observed at 286.7 and 289.2 eV, assigned to –C–O and –COOR, respectively, between SBE and SBE@C (500 °C). Furthermore, the characteristic diffraction peak assigned to C–H located at 287.6 eV completely vanished in SBE@C (500 °C), indicating that the volatile organic compounds on the surface of SBE were transformed into carbon species during pyrolysis at 500 °C. The results align with the outcomes of the FTIR analysis.

4. RESULTS AND DISCUSSION

4.1. Adsorption kinetics

To gain deeper insight into the adsorption kinetics of MB onto SBE or SBE@C (500 °C), the experimental data were fitted at 25, 35, and 45 °C using three kinetic adsorption models, namely, pseudo-first-order (Ho & McKay 1998), pseudo-second-order (Zhang *et al.* 2010), and intraparticle diffusion (Song *et al.* 2017) (Equations (2)–(4)) as shown in Figure 3:

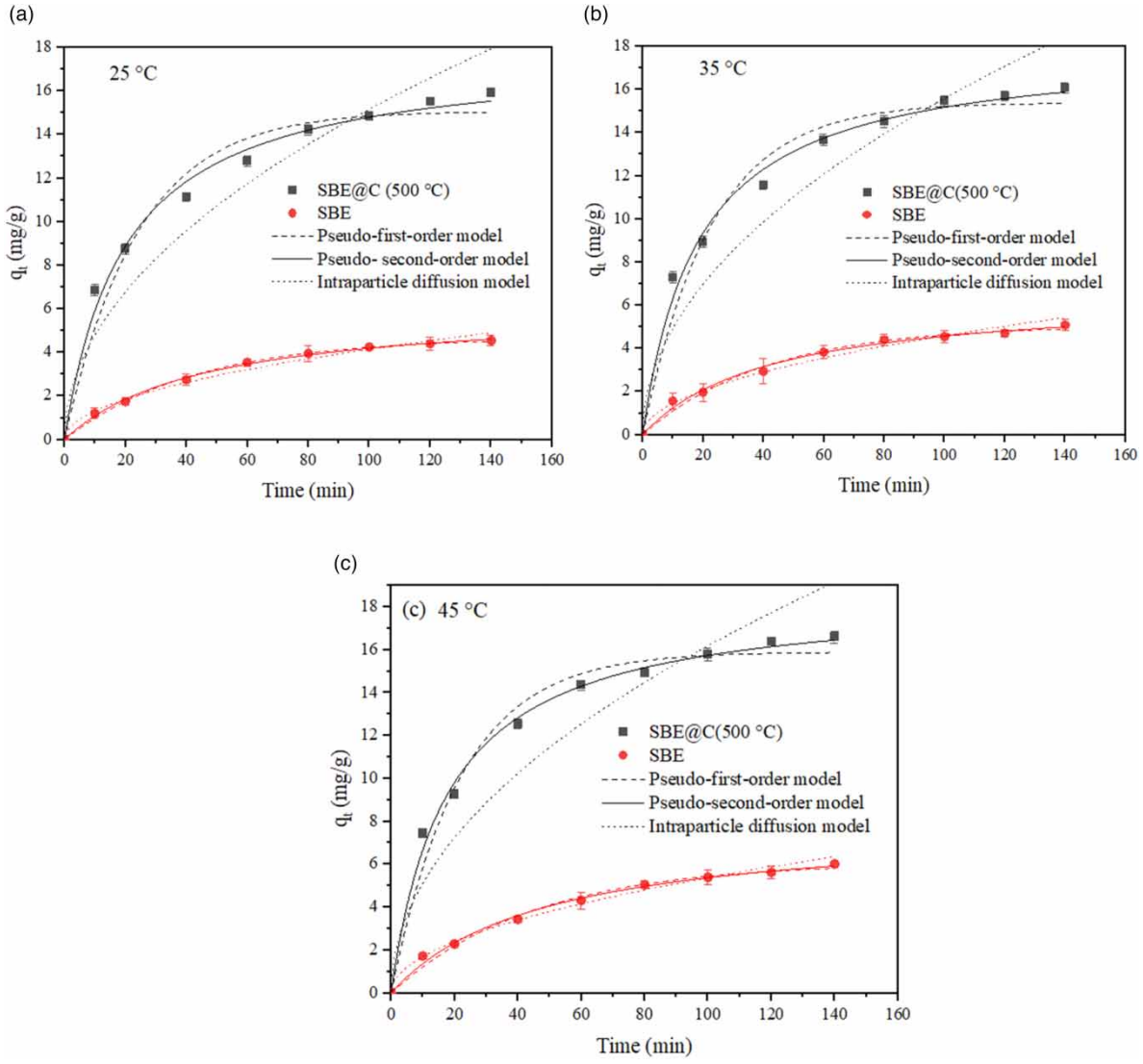

Figure 3 | Adsorption kinetics of MB onto SBE and SBE@C (500 °C) at (a) 25 °C, (b) 35 °C, and (c) 45 °C ($C_0 = 10$ mg/L, 150 rpm, and dosage = 0.6 g/L).

$$q_t = q_e(1 - e^{-k_1 t}) \tag{2}$$

$$q_t = \frac{k_2 q_e^2 t}{1 + k_2 q_e t} \tag{3}$$

$$q_t = k_3 t^{0.5} \tag{4}$$

The initial sorption rate v_o can be defined as:

$$v_o = K_1 q_e \tag{5}$$

$$v_o = K_2 q_e^2 \tag{6}$$

where q_t denotes the removal capacity of MB (mg/g) at time t (min); q_e represents the removal capacity of MB (mg/g) at equilibrium; and k_1, k_2, and k_3 are the rate constants (min^{-1}), (g/(mg min)), and (mg/(g $min^{1/2}$)), respectively.

As depicted in Figure 3(a) and 3(c), the SBE and SBE@C (500 °C) adsorption capacities increased from 4.55 to 6.02 mg/g and 15.93 to 16.59 mg/g (approximately 1.32 and 1.04 times), respectively, when the temperature increased from 25 to 45 °C. SBE@C (500 °C) reached equilibrium more quickly than SBE. For SBE@C (500 °C) at 45 °C, as shown in Figure 3(c), a significant increase in the adsorption capacity from 7.44 to 14.94 mg/g was observed as the contact time increased from 10 to 80 min. Initially, the enhanced removal capacity of MB by SBE@C (500 °C) was due to the presence of several active adsorption sites on the material surface. The removal capacity continued to increase, slightly increasing to 16.59 mg/g after 140 min of contact. Moreover, further extension of the contact time did not lead to a notable increase in the adsorption capacity, mainly due to the limited number of active adsorption sites on the material surface, with most of these sites already occupied by MB dye molecules (Deniz 2013). Table 1 shows the results of the experimental data and correlation coefficient (R^2) fitted to the three dynamic models.

Table 1 | The kinetic model fitting parameters of MB adsorption by SBE and SBE@C (500 °C) at 25, 35, and 45 °C

		Pseudo-first-order model					Pseudo-second-order model				Intraparticle diffusion model	
Adsorbent	T (°C)	q_e exp (mg/g)	q_e Cal (mg/g)	k_1 (min^{-1})	v_o (mg/(g min))	R^2	q_e Cal (mg/g)	k_2 (g/(mg min))	v_o (mg/(g min))	R^2	k_3 (mg/(g $min^{1/2}$))	R^2
SBE	25	4.552	4.686	0.023	0.11	0.997	6.213	0.003	0.12	0.997	0.420	0.980
	35	5.080	5.065	0.024	0.12	0.987	6.524	0.004	0.17	0.992	0.454	0.984
	45	6.020	6.092	0.022	0.13	0.989	7.962	0.003	0.19	0.994	0.537	0.978
SBE@C	25	15.925	15.08	0.042	0.63	0.970	17.752	0.003	0.95	0.991	1.516	0.920
(500 °C)	35	16.080	15.39	0.044	0.68	0.973	17.977	0.003	0.97	0.992	1.559	0.899
	45	16.589	15.90	0.046	0.73	0.981	18.537	0.003	1.03	0.995	1.618	0.888

In comparison to other kinetic models, the pseudo-second-order models of SBE and SBE@C (500 °C) had the highest correlation coefficients $R^2 \geq 0.992$ and $R^2 \geq 0.991$, respectively. These findings are in agreement with previous studies of MB adsorption onto activated carbon composited with Egyptian black sand (Elkholy *et al.* 2023), and MB adsorption by activated carbon from peanut shells (Sanou *et al.* 2024). This suggests that MB adsorption onto SBE or SBE@C (500 °C) involves chemisorption (Valentini *et al.* 2023). The initial sorption rate v_o was calculated using Equations (5) and (6). Based on the pseudo-second-order kinetics model, for SBE and SBE@C (500 °C) at 45 °C, there was an increase in v_o from 0.19 to 1.03 mg/(g min), respectively. Hence, the v_o for SBE@C (500 °C) increased by a factor of 5.42 after pyrolysis. The v_o for SBE and SBE@C (500 °C) increased with increasing temperature, indicating that an increase in temperature is beneficial for enhancing the v_o for MB adsorption by both materials.

4.2. Adsorption isotherms

Figure 4 shows the isothermal adsorption results of MB by SBE@C (500 °C) at 25, 35, and 45 °C and the equilibrium adsorption capacity of SBE and SBE@C (500 °C) at 45 °C. To gain deeper insight into the isothermal adsorption characteristics, the isothermal adsorption experimental data were fitted using the *Langmuir model* and the *Freundlich model* (Freundlich 1907; Langmuir 1918; Khitous *et al.* 2016).

As illustrated in Figure 4(a), the isotherm curves indicate a marginal increase in the MB removal capacity from 28.09 to 30.62 mg/g with increasing temperature from 25 to 45 °C. Figure 4(b) shows that the equilibrium adsorption capacity of SBE@C (500 °C) at 29.54 mg/g was approximately 2.8 times that of SBE at 10.62 mg/g. This is

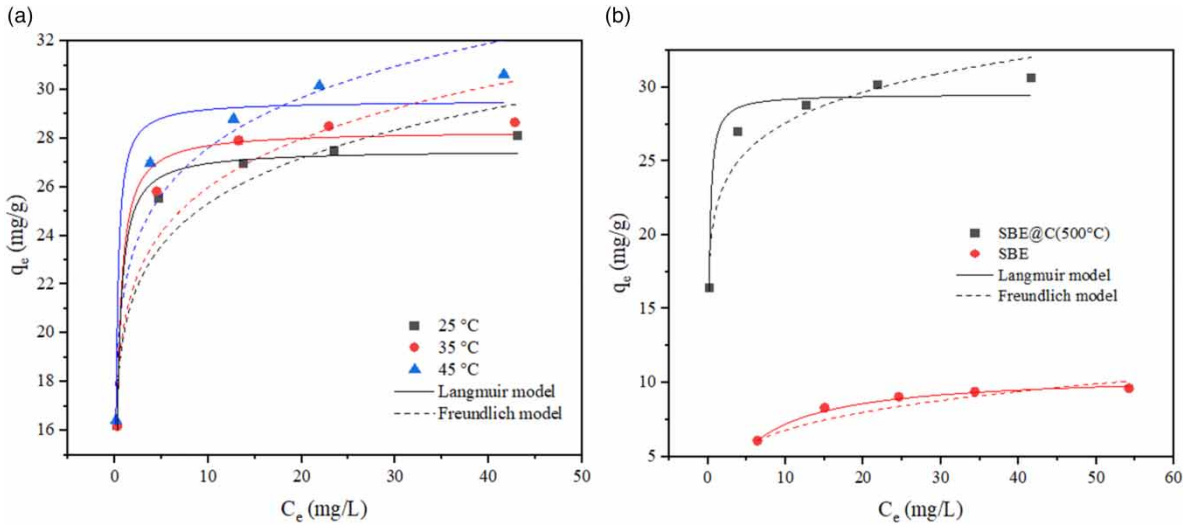

Figure 4 | Adsorption isotherms of MB onto (a) SBE@C (500 °C) at 25, 35, and 45 °C; (b) SBE and SBE@C (500 °C) at 45 °C.

primarily attributable to the significantly formed pore structure and increased specific surface area following the calcination of SBE, which is reflected in the SEM and BET results. Compared with other reported adsorbents of different activated materials (Supplementary Table S2), SBE@C (500 °C) has a satisfactory MB adsorption capacity. Table 2 shows the isotherm model fitting parameters of MB adsorption by both SBE and SBE@C (500 °C).

Table 2 | The isotherm model fitting parameters of MB adsorption by SBE and SBE@C (500 °C)

	Freundlich isotherm $q_e = K_F \times C_e^{1/n}$				Langmuir isotherm $q_e = \frac{Q_0 \times K_L \times C_e}{1 + K_L \times C_e}$		
	T (°C)	K_F (mg/g)(L/mg)$^{1/n}$	n	R^2	Q_0 (mg/g)	K_L (L/mg)	R^2
SBE	25	3.380	5.83	0.967	6.980	0.260	0.987
	35	3.310	4.38	0.994	8.980	0.190	0.999
	45	3.950	4.25	0.964	10.62	0.210	0.997
SBE@C (500 °C)	25	19.996	9.75	0.909	27.531	4.754	0.987
	35	20.310	9.35	0.905	28.312	4.493	0.984
	45	21.699	9.57	0.939	29.544	8.016	0.965

Based on the isothermal adsorption process, the correlation coefficients (R^2) for SBE and SBE@C (500 °C) of the *Langmuir* model were ≥0.987 and ≥0.965, respectively, and are better suited for describing the equilibrium MB removal than the *Freundlich* isotherm model, with correlation coefficients (R^2) for SBE and SBE@C (500 °C) ≥0.964 and ≥0.905, respectively as shown in Table 2. Hence, the adsorption of MB by SBE or SBE@C (500 °C) is attributed to monolayer adsorption (Wang *et al.* 2023). These findings are in agreement with previous studies on MB adsorption by low-cost adsorbent and MB adsorption onto synthesized activated carbon where the Langmuir model was found to be more accurate when compared with the Freundlich model (Al-Asadi *et al.* 2023; El Jery *et al.* 2024). Compared with SBE, SBE@C (500 °C) exhibited an enhanced adsorption ability for MB.

4.3. Adsorption thermodynamics

To better understand the mechanism of MB adsorption by SBE@C (500 °C), three important thermodynamic adsorption parameters, the Gibbs free energy ($\Delta G°$, kJ/mol), enthalpy ($\Delta H°$, kJ/mol), and entropy change ($\Delta S°$, J/mol), were calculated using Equations (7)–(9):

$$\Delta G = -RT \ln K_c \tag{7}$$

$$K_c = \frac{q_e}{C_e} \tag{8}$$

$$\Delta G^\circ = \Delta H^\circ - T\Delta S^\circ \tag{9}$$

where $R = 8.314$ (J/(mol K)) indicates the ideal gas constant; T denotes the temperature in K; K_c (L/mol) is the distribution coefficient; and C_e denotes the MB dye concentration at adsorption equilibrium in mg/L. Additionally, Equation (9) indicates that the $\Delta S°$ and $\Delta H°$ values are derived from the slope and intercept on the graph where T is plotted on the X-axis and $\Delta G°$ is plotted on the Y-axis.

Supplementary Table S3 shows the thermodynamic parameters for MB adsorption by SBE@C (500 °C). All the $\Delta G°$ values were <0, indicating a spontaneous adsorption process (Shahwan 2021). Moreover, the decreasing values of $\Delta G°$ with increasing temperature show that the MB adsorption process becomes more beneficial with increasing temperature (Golban *et al.* 2019). A positive $\Delta H°$ (26.39 kJ/mol) indicates an endothermic adsorption process. The ($\Delta S°$) value is positive (121.00 J/mol), indicating an increase in disorder or randomness of the MB removal process. These findings align with previous literature (Al-Mokhalelati *et al.* 2021).

4.4. Effect of pyrolysis temperature

The impact of pyrolysis temperature (300–900 °C) on MB removal from wastewater by pyrolyzed SBE was investigated. The results, as illustrated in Supplementary Figure S1, indicate that the untreated SBE has a very low adsorption capacity at equilibrium (2.55 mg/g). Pyrolysis at 300 °C resulted in incomplete carbonization of the surface oil of the material, leading to poor adsorption performance (1.83 mg/g). When the pyrolysis temperature is 500 °C, the removal capacity significantly increases to 10 mg/g due to the full carbonization of organic material on the SBE surface. However, at 700 and 900 °C, the temperature may be too high to preserve the internal pore structure of the material and could contribute to a decrease in its adsorption capacity (9.59 and 8.43 mg/g, respectively).

4.5. Effect of adsorbent dosage

The adsorbent dosage was varied (0.3–1.5 g/L) to investigate the impact of the SBE@C (500 °C) dosage on MB removal from wastewater, as shown in Supplementary Figure S3. The SBE@C (500 °C) removal efficiency (Supplementary Figure S3(a)) increased with increasing dosage (0.3 to 1.5 g/L) from 65.90 to 100%, respectively, after 120 min of contact. Compared with lower dosages of SBE@C (500 °C), higher dosages of SBE@C (500 °C) take less time to reach equilibrium due to the presence of multiple active adsorption sites (Zhang *et al.* 2018). As the SBE@C (500 °C) dose increased from 0.3 to 1.5 g/L, the matching adsorption capacity in Supplementary Figure S3(b) decreased from 21.97 to 6.90 mg/g, respectively. This is primarily because the adsorption sites on the adsorbent do not become saturated during the adsorption process. As a result, increasing the amount of adsorbent does not lead to a proportional increase in adsorption capacity (Chiban *et al.* 2016). These findings align with the results of a previous study (Ishak *et al.* 2021).

4.6. Effect of initial pH

The influence of initial pH on the equilibrium adsorption capacity of MB by SBE or SBE@C (500 °C) is illustrated in Supplementary Figure S4(a). The pH of the zero point of charge (pH_{pzc}) plots of SBE and SBE@C (500 °C) were also plotted, as illustrated in Supplementary Figure S4(b). The pH_{pzc} value is a key parameter that helps identify the type of active centers on the surface of a material. The pH at which the final pH was equal to the initial pH was considered the pH_{pzc}, indicating a neutral charge at this pH value. The pH_{pzc} values for SBE and SBE@C (500 °C) were determined to be 4.55 and 7.31, respectively. When the surface charge of SBE or SBE@C (500 °C) is negatively charged, it promotes the adsorption of cationic dyes (Bortoluz *et al.* 2020). The differences in pH_{pzc} values between these two materials could explain the observed differences in their adsorption capacities for MB.

With increasing pH (4–9), the removal capacities of both SBE and SBE@C (500 °C) increased from 3.49 to 4.71 mg/g and 15.4 to 16.50 mg/g, respectively, as shown in Supplementary Figure S4(a). The poor adsorption performance observed at pH values of 4 and 5 suggested that an abundance of H^+ ions competed with the MB cations for available adsorption sites. At a higher pH range (6–9), the surfaces of the SBE and SBE@C (500 °C) particles are more likely to acquire a negative charge, resulting in strong electrostatic attraction with the positively charged MB cations (Bulut & Aydin 2006). The increasing trend of the MB adsorption capacity became more stable for SBE and SBE@C (500 °C) at higher pH values (6–9); therefore, the pH was optimized at a pH of 8. The pH had a minimal impact on the adsorption process, making it advantageous for effective adsorption under real wastewater conditions. A comparable trend has been noted for the adsorption of MB onto papaya bark fibers (Nipa *et al.* 2023).

4.7. Effects of coexisting cations and cationic strength

There are many cations in wastewater contaminated with MB, and these cations greatly affect the removal efficiency of MB by adsorbents. To avoid adding more coexisting ions, neither an acid nor a base solution was used for pH control in the solution during the adsorption experiment. To gain deeper insight into the impacts of coexisting cations on MB adsorption by SBE or SBE@C (500 °C), five coexisting cation types were selected (0.01 mol/L Na^+, K^+, Mg^{2+}, Al^{3+}, and Fe^{3+}); the results are shown in Figure 5(a).

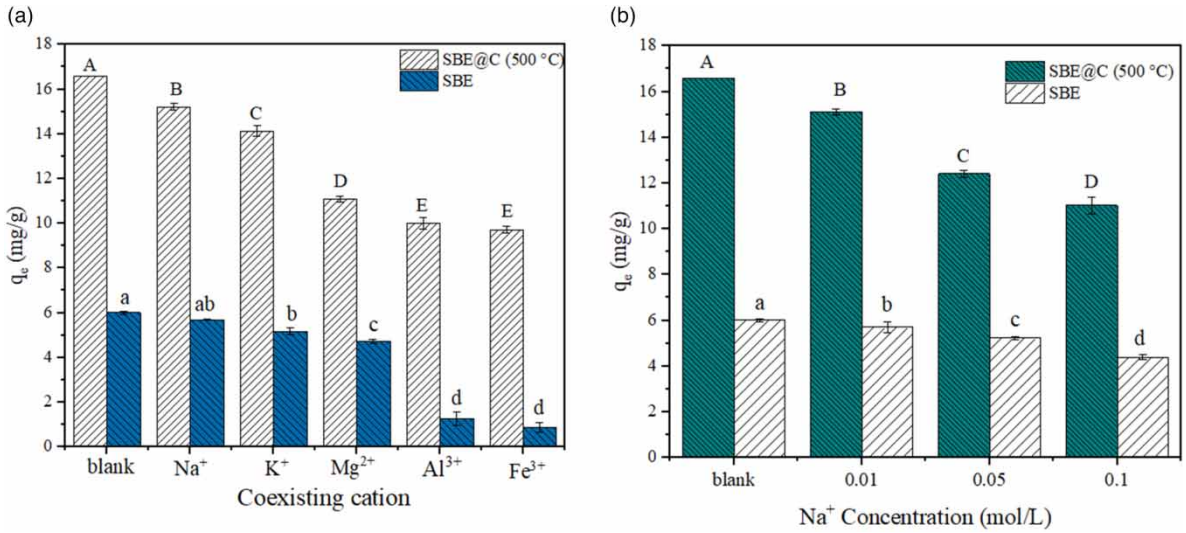

Figure 5 | Effects of (a) coexisting cations and (b) ionic strength (Na^+) for MB adsorption by SBE and SBE@C (500 °C) ($T = 25$ °C, $C_0 = 10$ mg/L, dosage = 0.6 g/L, and $V = 100$ mL).

SBE and SBE@C (500 °C) inhibited the MB removal rate in a similar order: $Fe^{3+} > Al^{3+} > Mg^{2+} > K^+ > Na^+$. Within 140 min, the ability of SBE and SBE@C (500 °C) to adsorb MB decreased from 5.70 to 0.87 mg/g and 15.21 to 9.71 mg/g, respectively, when MB coexisted with Na^+, K^+, Mg^{2+}, Al^{3+}, and Fe^{3+}. Compared with the blank experiment (6.01 and 16.6 mg/g) for SBE and SBE@C (500 °C), respectively, all these values were lower. The most significant impact was observed for Fe^{3+}, and the removal capacity of MB by SBE and SBE@C (500 °C) decreased from 6.01 to 0.87 mg/g and 16.60 to 9.71 mg/g, respectively, when the MB solution contained 0.01 mol/L Fe^{3+}, thereby almost inhibiting the removal of MB by SBE. The affinity of these cations for SBE and SBE@C (500 °C) may be the cause of their inhibitory effects on adsorption, as they compete for available adsorption sites between the cationic MB solution and the cations present on the adsorbent surface. It has been reported that cations with very small ionic radii have a greater tendency to enter adsorbent pores and can be adsorbed more readily than those with larger ionic radii. The ionic radii of K^+, Na^+, Mg^{2+}, Fe^{3+}, and Al^{3+} are 0.133, 0.097, 0.066, 0.064, and 0.051 nm, respectively (Kilislioglu 2003). Among the five cations, Fe^{3+} and Al^{3+} have the smallest ionic radii and are more readily adsorbed onto SBE and SBE@C (500 °C), thus forming a competitive relationship with MB. Higher valence states of Fe^{3+} and Al^{3+} had greater inhibitory effects on the SBE and SBE@C (500 °C) adsorption of MB than did Na^+, K^+, and Mg^{2+}.

The impact of varying concentrations of Na^+ (0.01, 0.05, and 0.1 mol/L) on the removal of MB by SBE and SBE@C (500 °C) was investigated to study the impact of cationic strength. Figure 5(b) shows that as the Na^+ concentration increased from 0.01 to 0.1 mol/L, the removal capacity of MB by both SBE and SBE@C (500 °C) decreased from 6.01 to 4.40 mg/g and 16.60 to 11.03 mg/g, respectively. These results indicate that higher Na^+ concentrations enhance the inhibitory effect of Na^+ on MB adsorption by SBE or SBE@C (500 °C); this is most likely due to increased competition between Na^+ and MB cations for available adsorption sites (Ren *et al.* 2020).

4.8. Regeneration

The reusability of SBE@C (500 °C) in removing MB from wastewater was evaluated using the desorption technique with 0.1 mol/L NaOH. The results, as illustrated in Figure 6(a), indicate that the removal capacity of

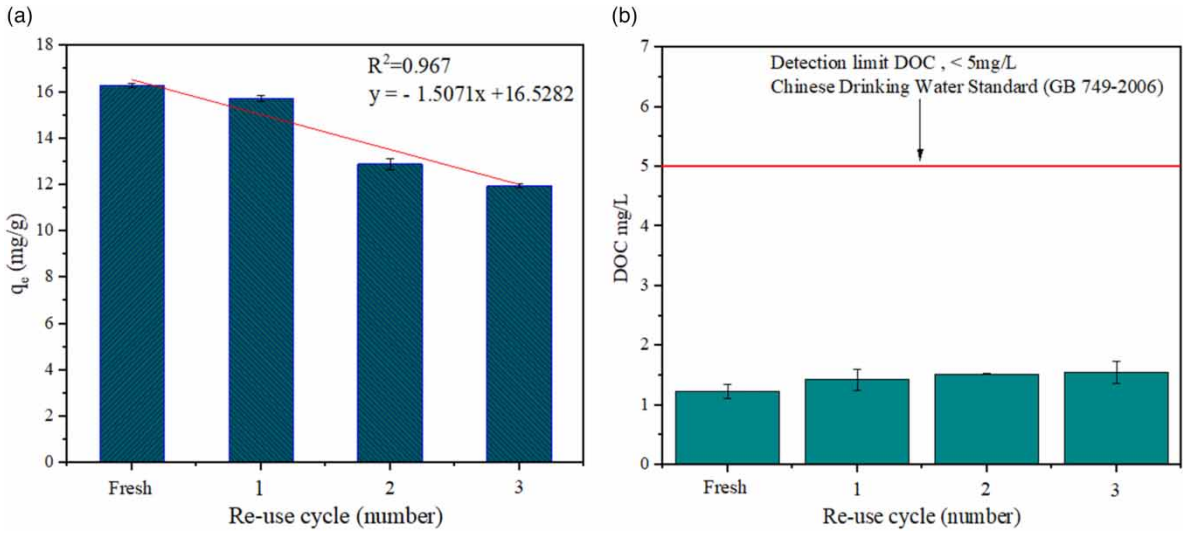

Figure 6 | (a) Reuse performance of SBE@C (500 °C) on the adsorption of MB and (b) DOC of MB solution at each reuse cycle (number) after MB adsorption by SBE@C (500 °C) ($T = 25$ °C, $C_0 = 10$ mg/L, dosage = 0.6 g/L, and $V = 100$ mL).

SBE@C (500 °C) slowly decreased with repeated usage, demonstrating a linear correlation ($R^2 = 0.967$) between the reuse cycle (number) and the adsorption capacity. After three reuse cycles, the removal capacity of SBE@C (500 °C)-de decreased from 16.29 to 11.94 mg/g. Compared with the fresh material, SBE@C (500 °C)-de retained 73.3% of its adsorption capacity. After 11 regeneration cycles, SBE@C (500 °C)-de is predicted to lose its adsorption capacity for MB. Therefore, SBE@C (500 °C) exhibited satisfactory reusability. Figure 6(b) shows the concentrations of DOC released into the MB solution for each reuse cycle (number) by SBE@C (500 °C) after adsorption. Figure 6(b) illustrates that the concentrations of DOC released into the MB solutions by SBE@C (500 °C) are very low, with the third reuse cycle (number) showing a slightly higher concentration of 1.55 mg/L, while the fresh SBE@C (500 °C) exhibited the lowest concentration of 1.23 mg/L. The concentrations of DOC released by the SBE@C (500 °C) at each reuse cycle (number) after the adsorption of MB satisfies China's drinking water quality standards (DOC < 5 mg/L, GB5749-2006, China), making it a feasible adsorbent for the practical removal of MB from wastewater without causing secondary pollution to the surrounding water environment. Additionally, Supplementary Figure S2 shows the concentrations of DOC released into pure water and the MB solution by SBE and SBE@C (500 °C) after adsorption. The levels of DOC released into the pure water and the MB solution by SBE were 10.12 and 14.19 mg/L, respectively. In comparison with SBE@C (500 °C), the DOC released into pure water and the MB solution was 0.8 and 1.23 mg/L, respectively. These values are significantly lower than those of SBE and meet China's drinking water quality standards. The concentration of DOC released by untreated SBE is considerably high and does not meet the standards for drinking water quality in China.

4.9. Adsorption mechanisms

Based on the premise that π–π interactions can occur between aromatic rings with π bonds in both the adsorbent and adsorbate (Wan *et al.* 2019), this study offers evidence that supports the presence of a π bond in the MB molecule (Supplementary Table S1). The FTIR results show a characteristic absorption band of aromatic carbon at 1,633 cm^{-1}, confirming the existence of a π bond in both SBE and SBE@C (500 °C). Therefore, it is concluded that the π–π interaction serves as a key mechanism for the adsorption of MB in this study. A study on the removal of MB dye by acid-fractionated biomass materials also found comparable outcomes (Jawad *et al.* 2020).

The pH_{pzc} for SBE and SBE@C (500 °C) were found to be 4.55 and 7.77, respectively (Supplementary Figure S4(b)). Supplementary Figure S4(a) shows that the adsorption capacity for SBE toward MB increases at pH > 5, and at pH > 6 for SBE@C (500 °C). The observed behavior can be attributed to the pH_{pzc} values, which indicate that at pH > 4.55 for SBE and pH > 7.77 for SBE@C (500 °C), the adsorbent surface acquires a complete negative charge. This negative charge facilitates stronger electrostatic interactions with positively charged MB molecules, leading to enhanced adsorption. The results of this study suggest that electrostatic interactions play a significant role in the adsorption of MB by SBE and SBE@C (500 °C). A similar study on

acid-factionalized biomass material for MB dye removal has found electrostatic interaction as a major driving force of MB adsorption (Jawad *et al.* 2020).

BET results revealed that SBE@C (500 °C) has a significantly larger specific surface area, and pore size compared with SBE (Supplementary Table S5). Specifically, the specific surface area significantly increased from 0.17 m^2/g (SBE) to 68.28 m^2/g (SBE@C (500 °C)), and the pore size increased from 13.83 for SBE to 19.93 for SBE@C (500 °C). With a minimum molecular cross-section of about 0.8 nm, the MB molecule is unable to enter pores smaller than 1.3 nm in diameter (Wang *et al.* 2005). Hence, the larger pore structures present in SBE@C (500 °C) allow for greater access of MB molecules, leading to a higher adsorption capacity compared with SBE.

5. CONCLUSIONS

In this study, SBE, a by-product of the oil refinery, was pyrolyzed under anoxic conditions to obtain SBE@C (500 °C). The results showed that the initial adsorption rate v_o at 45 °C increased from 0.19 mg/(g min) of SBE to 1.03 mg/(g min) of SBE@C (500 °C), while the maximum adsorption capacity of MB, Q_0 (determined by the Langmuir model), significantly increased from 10.62 mg/g of SBE to 29.54 mg/g of SBE@C (500 °C). The adsorption kinetics of MB by SBE@C (500 °C) can be effectively described with the pseudo-second-order model ($R^2 \geq$ 0.991). In addition, after three regeneration cycles, SBE@C (500 °C) retained 73.3% of its adsorption capacity, and it regenerated 11 times before its adsorption performance completely decreased. The findings from the study showed that the DOC released by SBE@C (500 °C) is minimal and meets China's drinking water quality requirements, making it a feasible adsorbent for the practical removal of MB from wastewater without causing secondary pollution to the surrounding water environment. The mechanism of MB adsorption onto SBE@C (500 °C) primarily involved π–π interactions, electrostatic interaction, and changes in physicochemical properties. In summary, this research offers a sustainable method for producing an efficient eco-friendly clay/carbon adsorbent that does not cause secondary pollution.

FUNDING

This study was supported by the National Natural Science Foundation of China (Nos. 52070073 and 52200013), the Science & Technology Innovation Talents in Universities of Henan Province (No. 22HASTIT009), the Key Projects of Scientific and Technological Collaborative Innovation of Zhengzhou City (No. 21ZZXTCX05), and the Innovative Funds Plan of Henan University of Technology (No. 2021ZKCJ09).

DATA AVAILABILITY STATEMENT

All relevant data are included in the paper or its Supplementary Information.

CONFLICT OF INTEREST

The authors declare there is no conflict.

REFERENCES

Abdelbasir, S. M., Shehab, A. I. & Khalek, M. A. A. (2023) Spent bleaching earth; recycling and utilization techniques: A review, *Resources, Conservation and Recycling Advances*, **17**, 200124. doi:10.1016/j.rcradv.2022.200124.

Al-Asadi, S. T., Al-Qaim, F. F., Al-Saedi, H. F. S., Deyab, I. F., Kamyab, H. & Chelliapan, S. (2023) Adsorption of methylene blue dye from aqueous solution using low-cost adsorbent: Kinetic, isotherm adsorption, and thermodynamic studies, *Environmental Monitoring and Assessment*, **195** (6), 676. doi:10.1007/s10661-023-11334-2.

Alharby, N. F., Almutairi, R. S. & Mohamed, N. A. (2021) Adsorption behavior of methylene blue dye by novel crosslinked O-CM-chitosan hydrogel in aqueous solution: Kinetics, isotherm and thermodynamics, *Polymers*, **13** (21), 3659. doi:10.3390/polym13213659.

Al-Mokhalelati, K., Al-Bakri, I. & Al Shibeh Al Wattar, N. (2021) Adsorption of methylene blue onto sugarcane bagasse-based adsorbent materials, *Journal of Physical Organic Chemistry*, **34** (7), 961671. doi:10.1002/poc.4193.

Bortoluz, J., Ferrarini, F., Bonetto, L.R., da Silva Crespo, J. & Giovanela, M. (2020) Use of low-cost natural waste from the furniture industry for the removal of methylene blue by adsorption: Isotherms, kinetics and thermodynamics, *Cellulose*, **27** (11), 6445–6466. doi:10.1007/s10570-020-03254-y.

Bulut, Y. & Aydin, H. (2006) A kinetics and thermodynamics study of methylene blue adsorption on wheat shells, *Desalination*, **194** (1–3), 259–267. doi:10.1016/j.desal.2005.10.032.

Chiban, M., Carja, G., Lehutu, G. & Sinan, F. (2016) Equilibrium and thermodynamic studies for the removal of As(V) ions from aqueous solution using dried plants as adsorbents, *Arabian Journal of Chemistry*, **9**, S988–S999. doi:10.1016/j.arabjc.2011.10.002.

Christidis, G. E., Scott, P. W. & Dunham, A. C. (1997) Acid activation and bleaching capacity of bentonites from the islands of Milos and Chios, Aegean, Greece, *Applied Clay Science*, **12** (4), 329–347. doi:10.1016/S0169-1317(97)00017-3.

Deniz, F. (2013) Adsorption properties of low-cost biomaterial derived from *Prunus amygdalus* L. for dye removal from water, *The Scientific World Journal*, **2013**, e4193. doi:10.1155/2013/961671.

Duman, O., Polat, T. G., Diker, C. Ö. & Tunç, S. (2020) Agar/κ-carrageenan composite hydrogel adsorbent for the removal of methylene blue from water, *International Journal of Biological Macromolecules*, **160**, 823–835. doi:10.1016/j.ijbiomac.2020.05.191.

El Jery, A., Alawamleh, H. S. K., Sami, M. H., Abbas, H. A., Sammen, S. S., Ahsan, A., Imteaz, M. A., Shanableh, A., Shafiquzzaman, Md, Osman, H. & Al-Ansari, N. (2024) Isotherms, kinetics and thermodynamic mechanism of methylene blue dye adsorption on synthesized activated carbon, *Scientific Reports*, **14** (1), 970. doi:10.1038/s41598-023-50937-0.

Elkholy, A. S., Yahia, M. S., Elnwawy, M. A., Gomaa, H. A. & Elzaref, A. S. (2023) Synthesis of activated carbon composited with Egyptian black sand for enhanced adsorption performance toward methylene blue dye, *Scientific Reports*, **13** (1), 4209. doi:10.1038/s41598-023-28556-6.

Freundlich, H. (1907) Über die adsorption in lösungen, *Zeitschrift für Physikalische Chemie*, **57U** (1), 385–470. doi:10.1515/zpch-1907-5723.

Golban, A., Lupa, L., Cocheci, L. & Pode, R. (2019) Synthesis of MGFE layered double hydroxide from iron-containing acidic residual solution and its adsorption performance, *Crystals*, **9** (10), 514. doi:10.3390/cryst9100514.

Heymann, K., Lehmann, J., Solomon, D., Schmidt, M. W. I. & Regier, T. (2011) C1s K-edge near edge X-ray absorption fine structure (NEXAFS) spectroscopy for characterizing functional group chemistry of black carbon, *Organic Geochemistry*, **42** (9), 1055–1064. doi:10.1016/j.orggeochem.2011.06.021.

Ho, Y. S. & McKay, G. (1998) Sorption of dye from aqueous solution by peat, *Chemical Engineering Journal*, **70** (2), 115–124. doi:10.1016/S1385-8947(98)00076-X.

Ishak, Z., Salim, S. & Kumar, D. (2021) Adsorption of methylene blue and reactive black 5 by activated carbon derived from tamarind seeds, *Tropical Aquatic and Soil Pollution*, **2** (1), 1–12. doi:10.53623/tasp.v2i1.26.

Jawad, A. H., Abdulhameed, A. S. & Mastuli, M. S. (2020) Acid-factionalized biomass material for methylene blue dye removal: A comprehensive adsorption and mechanism study, *Journal of Taibah University for Science*, **14** (1), 305–313. doi:10.1080/16583655.2020.1736767.

Kadi, S., Lellou, S., Marouf-Khelifa, K., Schott, J., Gener-Batonneau, I. & Khelifa, A. (2012) Preparation, characterisation and application of thermally treated Algerian halloysite, *Microporous and Mesoporous Materials*, **158**, 47–54. doi:10.1016/j.micromeso.2012.03.014.

Ke, Y., Zhu, X., Si, S., Zhang, T., Wang, J. & Zhang, Z. (2023) A novel adsorbent of attapulgite & carbon composites derived from spent bleaching earth for synergistic removal of copper and tetracycline in water, *International Journal of Environmental Research and Public Health*, **20** (2), 1573. doi:10.3390/ijerph20021573.

Khitous, M., Salem, Z. & Halliche, D. (2016) Removal of phosphate from industrial wastewater using uncalcined MgAl-NO_3 layered double hydroxide: Batch study and modeling, *Desalination and Water Treatment*, **57** (34), 15920–15931. doi:10.1080/19443994.2015.1077745.

Kilislioglu, A. (2003) The effect of various cations and pH on the adsorption of U(VI) on Amberlite IR-118H resin, *Applied Radiation and Isotopes*, **58** (6), 713–717. doi:10.1016/S0969-8043(03)00116-7.

Lagiewka, J., Nowik-Zajac, A., Pajdak, A. & Zawierucha, I. (2023) A novel multifunctional β-cyclodextrin polymer as a promising sorbent for rapid removal of methylene blue from aqueous solutions, *Carbohydrate Polymers*, **307**, 120615. doi:10.1016/j.carbpol.2023.120615.

Langmuir, I. (1918) The adsorption of gases on plane surfaces of glass, mica and platinum, *Journal of the American Chemical Society*, **40** (9), 1361–1403. doi:10.1021/ja02242a004.

Liu, L., Li, Y., Yoza, B.A., Hao, K., Li, Q.X., Li, Y., Wang, Q., Guo, S. & Chen, C. (2020) A char-clay composite catalyst derived from spent bleaching earth for efficient ozonation of recalcitrants in water, *Science of the Total Environment*, **699**, 134395. doi:10.1016/j.scitotenv.2019.134395.

Liu, Y., Chen, Y., Shi, Y., Wan, D., Chen, J. & Xiao, S. (2021) Adsorption of toxic dye Eosin Y from aqueous solution by clay/carbon composite derived from spent bleaching earth, *Water Environment Research*, **93** (1), 159–169. doi:10.1002/wer.1376.

Loutfi, M., Mariouch, R., Mariouch, I., Belfaquir, M. & ElYoubi, M. S. (2023) Adsorption of methylene blue dye from aqueous solutions onto natural clay: Equilibrium and kinetic studies, *Materials Today: Proceedings*, **72**, 3638–3643. doi:10.1016/j.matpr.2022.08.412.

Mana, M., Ouali, M.S. & Lindheimer, M. & Menorval, L. C. de (2008) Removal of lead from aqueous solutions with a treated spent bleaching earth, *Journal of Hazardous Materials*, **159** (2–3), 358–364. doi:10.1016/j.jhazmat.2008.02.079.

Mohadesi, M., Gouran, A., Darabi, F. & Samimi, M. (2024) Sunflower seed pulp ash as an efficient and eco-friendly adsorbent for Congo red uptake: Characteristics, kinetics, and optimization, *Water Practice and Technology*, **19** (1), 228–240. doi:10.2166/wpt.2023.224.

Nipa, S. T., Shefa, N. R., Parvin, S., Khatun, M. A., Alam, M. J., Chowdhury, S., Khan, M. A. R., Shawon, S. M. A. Z., Biswas, B. K. & Rahman, M. W. (2023) Adsorption of methylene blue on papaya bark fiber: Equilibrium, isotherm and kinetic perspectives, *Results in Engineering*, **17**, 100857. doi:10.1016/j.rineng.2022.100857.

Nurani, D. A., Anisa, N., Khatrin, I., Yasmine, Kadja, G. T. M. & Krisnandi, Y. K. (2024) Breathable iron-based MIL-88 framework as dye adsorbent in aqueous solution, *Chemistry (Switzerland)*, **6** (2), 283–298. doi:10.3390/chemistry6020015.

Qi, J., Hou, Y., Hu, J., Ruan, W., Xiang, Y. & Wei, X. (2020) Decontamination of methylene blue from simulated wastewater by the mesoporous rGO/Fe/Co nanohybrids: Artificial intelligence modeling and optimization, *Materials Today Communications*, **24**, 100709. doi:10.1016/j.mtcomm.2019.100709.

Raj, D. V. K., Devi, M. R., Venkatesh, B., Kumar, S. K. S. & Prakash, C. (2024) Sustainable removal of methylene blue dye from textile effluent by using cellulose nanocrystals extracted from sugarcane bagasse, *Biomass Conversion and Biorefinery*, **14** (10), 11539–11547. doi:10.1007/s13399-022-03284-5.

Ren, S., Meng, Z., Sun, X., Lu, H., Zhang, M., Lahori, A. H. & Bu, S. (2020) Comparison of Cd^{2+} adsorption onto amphoteric, amphoteric-cationic and amphoteric-anionic modified magnetic bentonites, *Chemosphere*, **239**, 124840. doi:10.1016/j.chemosphere.2019.124840.

Sanou, I., Bamogo, H., Sanou, A., Ouedraogo, M., Saadi, L., Waqif, M. & Millogo, Y. (2024) Adsorption of methylene blue in aqueous medium by activated carbon from peanut shells, *Chemistry Africa*. **7** (5), 2777–2794. doi:10.1007/s42250-024-00927-0.

Shahwan, T. (2021) Critical insights into the limitations and interpretations of the determination of ΔG^{o}, ΔH^{o}, and ΔS^{o} of sorption of aqueous pollutants on different sorbents, *Colloids and Interface Science Communications*. **41**, 100369 doi:10.1016/j.colcom.2021.100369.

Song, W., Gao, B., Wang, H., Xu, X., Xue, M., Zha, M. & Gong, B. (2017) The rapid adsorption-microbial reduction of perchlorate from aqueous solution by novel amine-crosslinked magnetic biopolymer resin, *Bioresource Technology*, **240**, 68–76. doi:10.1016/j.biortech.2017.03.064.

Tang, J., Zong, L., Mu, B., Zhu, Y. & Wang, A. (2018) Preparation and cyclic utilization assessment of palygorskite/carbon composites for sustainable efficient removal of methyl violet, *Applied Clay Science*, **161**, 317–325. doi:10.1016/j.clay.2018.04.039.

Valentini, F., Cerza, E., Campana, F., Marrocchi, A. & Vaccaro, L. (2023) Efficient synthesis and investigation of waste-derived adsorbent for water purification. Exploring the impact of surface functionalization on methylene blue dye removal, *Bioresource Technology*, **390**, 129847. doi:10.1016/j.biortech.2023.129847.

Wan, D., Wu, L., Liu, Y., Chen, J., Zhao, H. & Xiao, S. (2019) Enhanced adsorption of aqueous tetracycline hydrochloride on renewable porous clay-carbon adsorbent derived from spent bleaching earth via pyrolysis, *Langmuir*, **35** (11), 3925–3936. doi:10.1021/acs.langmuir.8b04179.

Wan, D., Cheng, X., Shi, Y., Chen, Z., Liu, Yongde, Han, X., Liu, Yongzhi & Zhang, Z. (2021) Insights into lead removal in water using a novel carbonized material derived from the by-product of oil refining: Action mechanism and performance optimization, *Journal of Chemical Technology and Biotechnology*, **96** (11), 3224–3236. doi:10.1002/jctb.6879.

Wang, S., Zhu, Z. H., Coomes, A., Haghseresht, F. & Lu, G. Q. (2005) The physical and surface chemical characteristics of activated carbons and the adsorption of methylene blue from wastewater, *Journal of Colloid and Interface Science*, **284** (2), 440–446. doi:10.1016/j.jcis.2004.10.050.

Wang, X., Zhang, A., Chen, M., Seliem, M. K., Mobarak, M., Diao, Z. & Li, Z. (2023) Adsorption of azo dyes and Naproxen by few-layer MXene immobilized with dialdehyde starch nanoparticles: Adsorption properties and statistical physics modeling, *Chemical Engineering Journal*, **473**, 145385. doi:10.1016/j.cej.2023.145385.

Wu, X., Gao, P., Zhang, X., Jin, G., Xu, Y. & Wu, Y. (2014) Synthesis of clay/carbon adsorbent through hydrothermal carbonization of cellulose on palygorskite, *Applied Clay Science*, **95**, 60–66. doi:10.1016/j.clay.2014.03.010.

Zhang, S., Li, X. y. & Chen, J. P. (2010) Preparation and evaluation of a magnetite-doped activated carbon fiber for enhanced arsenic removal, *Carbon*, **48** (1), , 60–67. doi:10.1016/j.carbon.2009.08.030.

Zhang, X., Zhang, L. & Li, A. (2018) Eucalyptus sawdust derived biochar generated by combining the hydrothermal carbonization and low concentration KOH modification for hexavalent chromium removal, *Journal of Environmental Management*, **206**, 989–998. doi:10.1016/j.jenvman.2017.11.079.

Zhou, H. M., Qiao, X. C. & Yu, J. G. (2013) Influences of quartz and muscovite on the formation of mullite from kaolinite, *Applied Clay Science*, **80–81**, 176–181. doi:10.1016/j.clay.2013.04.004.

First received 3 July 2024; accepted in revised form 1 September 2024. Available online 12 September 2024